

A nalysis of energy- and tim e-dependence of supernova shock e ffects on neutrino crossing probabilities

G L. Fogli,¹ E. Lisi,¹ D. M ontanino,² and A. M irizzi¹

¹ D ipartimento di Fisica and Sezione INFN di Bari
Via Amendola 173, 70126 Bari, Italy

² D ipartimento di Scienza dei M ateriali and Sezione INFN di Lecce
Via Amesano, 73100 Lecce, Italy

Abstract

It has recently been realized that supernova neutrino signals may be affected by shock propagation over a time interval of a few seconds after bounce. In the standard three-neutrino oscillation scenario, such effects crucially depend on the neutrino level crossing probability P_H in the 1-3 sector. By using a simplified parametrization of the time-dependent supernova radial density profile, we show explicitly that simple analytical expressions for P_H accurately reproduce the phase-averaged results of numerical calculations in the relevant parameter space. Such expressions are then used to study the structure of P_H as a function of energy and time, with particular attention to cases involving multiple crossing along the shock profile. Illustrative applications are given in terms of positron spectra generated by supernova electron antineutrinos through inverse beta decay.

PACS numbers: 14.60.Pq, 13.15.+g, 97.60.Bw

I. INTRODUCTION

The realization that the supernova shock propagation can affect neutrino flavor transitions [1] a few seconds after core bounce [2] is gaining increasing attention in the recent literature on supernova neutrinos [3, 4, 5, 6, 7, 8, 9, 10]. Indeed, time-dependent variations of the neutrino potential in matter [11] along the supernova shock profile can leave an interesting imprint on the energy and time structure of the (anti)neutrino signal at the Earth [1, 8, 10]. Observation of such possible effects, although very challenging from an experimental viewpoint, would open a unique opportunity to study some aspects of the supernova shock dynamics in "real time." Moreover, the strong sensitivity of such effects to the neutrino oscillation parameters [1, 8, 10] might, in principle, provide us with additional constraints (or hints, at least) on the neutrino mass spectrum and mixing angles.

From a conservative viewpoint, it should be stressed that current simulations of core-collapse supernovae, despite remarkable efforts, may still require substantial physics improvements [12]. It is not excluded that more refined simulations might significantly modify, e.g., the main features of shock profile discussed in [1], and especially its propagation velocity and density gradient, which govern the structure of the neutrino crossing probabilities [1, 8, 10]. Moreover the time and energy dependence of the source (anti)neutrino fluxes might be more complicated and uncertain [13, 14] than is customarily assumed, making it more difficult to identify shock-related signals. All these potential systematic uncertainties in the basic physics ingredients might be large enough to weaken the significance of shock-related signals, even with hypothetically large experimental statistics. However, despite all these caveats, the stakes are so high that further investigations on possible shock effects on supernova neutrinos are widely justified, in our opinion.

The purpose of this work is to investigate in some detail the energy- and time-dependence of the neutrino crossing probabilities along the supernova shock. We assume the active 3-oscillation scenario (Sec. II), and construct an empirical parametrization for the shock profile (Sec. III). Analytical calculations are shown to reproduce well (and to be much more convenient than) numerical approaches to the overall crossing probabilities, and are used to break down the multiple transition structure along the shock density profile, both in the energy domain (Sec. IV) and in the time domain (Sec. V). Finally, applications are given in terms of antineutrino event spectra observable at the Earth through inverse beta decay (Sec. VI). Conclusions and prospects for further work are given in Sec. VII.

The bottom line of our work is that simple, analytical calculations of the crossing probabilities along the supernova shock profile appear to be adequate to study the structure of neutrino flavor transitions in the energy and time domain, for all practical purposes. The specific probability values estimated in this work, however, should not be taken too literally, being based on a simplified description of the matter density profile, which is subject to change as more detailed supernova shock simulations are performed and become publicly available.

II. 3 FRAMEWORK: NOTATION AND ANALYTICAL APPROXIMATIONS

Throughout this work, we consider only flavor transitions among the three known active neutrinos ν_e , ν_μ , and ν_τ . In the following, we set the notation and briefly describe the analytical expressions for the crossing probabilities.

The squared mass spectrum is parameterized as

$$(m_1^2; m_2^2; m_3^2) = \left(\frac{m^2}{2}; + \frac{m^2}{2}; \pm m^2 \right); \quad (1)$$

where the sign in front of m^2 distinguishes the cases of normal (+) and inverted (-) hierarchy. The mixing matrix U is defined in terms of three rotation angles θ_{ij} , ordered as for the quark mixing matrix [15],

$$U = U(\theta_{12}; \theta_{13}; \theta_{23}); \quad (2)$$

When needed, we take

$$\begin{aligned} m^2 = eV^2 &= 7.3 \cdot 10^5; & (3) \\ \sin^2 \theta_{12} &= 0.315; & (4) \end{aligned}$$

corresponding to the so-called LMA-I fit to the solar and reactor neutrino data [6]. We also take

$$m^2 = 3 \cdot 10^3 \text{ eV}^2; \quad (5)$$

close to the best fit to the atmospheric and accelerator neutrino data detected in Super-Kamiokande [17]. The value of $\sin^2 \theta_{23}$ is basically irrelevant for supernova neutrinos, since it corresponds to an unobservable rotation in the ($\nu_\mu; \nu_\tau$) flavor subspace. Concerning the mixing parameter $\sin^2 \theta_{13}$, we will pick up several representative values, well below the current 3 σ upper limit ($\sin^2 \theta_{13} < 0.05$ [17]).

The mass gap hierarchy ($m^2 = m^2 \pm 1$) and the smallness of $\sin^2 \theta_{13}$ guarantee, to a very good approximation, the factorization of the 3 neutrino dynamics into a "low" (L) and a "high" (H) 2 subsystem, whose dominant oscillation parameters are ($m^2; \theta_{12}$) and ($m^2; \theta_{13}$), respectively (see [18] and references therein). The corresponding neutrino wavenumbers are defined as

$$k_L = \sqrt{m^2 - 2E}; \quad (6)$$

$$k_H = \sqrt{m^2 + 2E}; \quad (7)$$

where E is the neutrino energy.

Potentially large matter effects [11] are expected when either k_L or k_H take values close to the neutrino potential V in matter,

$$V = \frac{P}{2} \bar{G}_F N_e(x); \quad (8)$$

where N_e is the electron density at the supernova radius x . In appropriate units,

$$\frac{V(x)}{eV^2 = M \text{ eV}} = 7.6 \cdot 10^8 Y_e \frac{(x)}{g = \text{cm}^3}; \quad (9)$$

where Y_e is the electron/nucleon number fraction (that we assume equal to 1/2), while $\rho(x)$ is the radial mass density profile. In particular, if the condition

$$V(x_H) = k_H \quad (10)$$

occurs at some point x_H , there is a finite probability P_H of crossing between effective mass eigenstates in the H subsystem, which is given to a good approximation by

$$P_H = \frac{\exp(2 r_H k_H \cos^2 \theta_{13}) - 1}{\exp(2 r_H k_H) - 1}; \quad (11)$$

for both neutrinos and antineutrinos (see [19] and related bibliography therein), with

$$r_H = \frac{d \ln V(x)}{dx} \Big|_{x=x_H}^{-1}; \quad (12)$$

For all the $V(x)$ profiles and $\sin^2 \theta_{13}$ values that will be used in the following, the above formula reduces to the well-known Landau-Zener (LZ) limit

$$P_H \approx \exp(-2 r_H k_H \sin^2 \theta_{13}) \quad (13)$$

at any energy of practical interest. In principle, the occurrence of the condition $k_L = V(x_L)$ at some radius x_L could also induce neutrino level crossing in the L subsystem with probability P_L (generally different for neutrinos and antineutrinos, see, e.g., [20]). However, for $\sin^2 \theta_{12}$ as large as in Eq. (4) it turns out that

$$P_L(\nu) \approx 0 \approx P_L(\bar{\nu}) \quad (14)$$

(adiabatic L-transitions), unless the density gradient explodes at $x = x_L$ (see also Sec. IV C).

The analytical form for the ν_e survival probability P_{ee} [19, 20] becomes then exceedingly simple (up to Earth matter effects)¹:

$$P_{ee} \approx \begin{cases} \sin^2 \theta_{12} P_H & (\nu; \text{normal}); \\ \cos^2 \theta_{12} & (\bar{\nu}; \text{normal}); \\ \sin^2 \theta_{12} & (\nu; \text{inverted}); \\ \cos^2 \theta_{12} P_H & (\bar{\nu}; \text{inverted}); \end{cases} \quad (15)$$

where "normal" and "inverted" refer to the hierarchy type for the mass spectrum. In the above equation, we have kept only the leading (exponential) θ_{13} -dependence [through Eq. (13)], and have neglected small additive terms of $O(\sin^2 \theta_{13})$, which are not relevant for our discussion. From the above equations, it appears that P_H can modulate the (otherwise constant) survival probability of ν_e in normal hierarchy and of $\bar{\nu}_e$ in inverted hierarchy, thus providing an important handle to solve the current hierarchy ambiguity.

The calculation of P_H is not entirely trivial in the presence of non-monotonic density profiles, where the condition in Eq. (10) can occur at several radii x_i , leading to multiple H-transitions; in particular, for the shock profiles studied in [1, 8], up to three transitions can occur:

$$V(x_i) = k_H \quad (i = 1; 2; 3); \quad (16)$$

where the points x_i are conventionally ordered as

$$x_1 < x_2 < x_3; \quad (17)$$

¹ Examples of Earth matter effects will be illustrated in Sec. VI.

The corresponding crossing probabilities are denoted as P_1 , P_2 , and P_3 . The P_i 's can be analytically calculated as in Eq. (13), with the inverse log-derivative r_i [Eq. (12)] evaluated at the point x_i .

If we assume that all relative neutrino phases can be averaged away, and that the three transitions can be exactly factorized, the overall crossing probability P_H can be defined in terms of a simple matrix equation [18]

$$\begin{pmatrix} 1 & P_H & P_H \\ P_H & 1 & P_H \end{pmatrix}^{-1} = \prod_{i=1}^3 \begin{pmatrix} 1 & P_i & P_i \\ P_i & 1 & P_i \end{pmatrix}^{-1}; \quad (18)$$

whose solution is

$$P_H = P_1 + P_2 + P_3 - 2(P_1P_2 + P_2P_3 + P_3P_1) + 4P_1P_2P_3; \quad (19)$$

We will refer to this simple equation for our analytical calculations of P_H .

Although the smallness of θ_{13} implies that each of the three transitions $P_{1,2,3}$ is (in general) well localized and can thus be separated from the others, the intrinsic accuracy of the factorization in Eq. (18) is not obvious a priori in the whole relevant parameter space. There are zones of the shock profile where two transitions can merge, or where the local density shape can be strongly different from the static, quasi-cubic power law which was used in [19] to test the analytical recipe of Eq. (11). Moreover, in the presence of multiple (interfering) transition amplitudes, it is worth checking that reasonable phase averaging effectively reproduces the incoherent factorization implicit in Eq. (18).

For such reasons, we think it useful to compare the analytical calculations of P_H [based on Eqs. (13) and (19)] with the results of a numerical (Runge-Kutta) evolution of the neutrino flavor propagation equations along representative shock density profiles. To our knowledge, such reassuring comparison has not been explicitly performed in the available literature.² In order to do so in both the time and energy domain (Secs. IV and V, respectively), we need a parametrization of the shock wave profile which is continuous in both the radius x and in post-bounce time t . Unfortunately, a similar parametrization (or, equivalently, a dense numerical table) is not publicly available; only some representative profiles are graphically reported in [1] and [8].³ In the following section, we thus introduce a simplified parametrization of the supernova density profile which is continuous in the $(x;t)$ variables. Such empirical profile captures the main qualitative features of the time and radial dependence of the (supposed spherically symmetric) shock propagation, allowing us to perform a meaningful comparison of numerical and analytical results, and to break down explicitly the analytical calculation of P_H into its three components P_1 , P_2 , and P_3 . Needless to say, such a simplified profile can and must be improved when more informative or refined supernova shock simulations become available.

A final remark is in order. In this work we are mainly concerned with the factorization of transition within the H subsystem, since the factorization between the L and H subsystems is guaranteed for θ_{12}^2 as low as in Eq. (3). However, small corrections to the L-H factorization

² The authors of Refs. [8] and [1] seem to have used a fully numerical and a mixed numerical+analytical approach to the neutrino evolution equations, respectively. The authors of Ref. [10] discuss only qualitatively the analytic form of P_3 , in the hypothesis that $P_1 \approx 0 \approx P_2$.

³ Notice that the bilogarithmic scales used in [1, 8] make it difficult to recover potentially interesting shock details by graphical reduction.

might arise for values of $m^2 \ll 10^4 \text{ eV}^2$ (see, e.g., [18] for earlier discussions and [10, 21] for more recent considerations). The analysis of these possible small corrections is beyond the scope of this work.

III. EMPIRICAL PARAMETRIZATION OF THE SHOCK DENSITY PROFILE

In this section we introduce a simplified, empirical parametrization of the shock density profile, which reproduces the main features of the graphical profile in [1] and, at same time, is continuous in both x and t . In this way, numerical and analytical calculations of P_H can continuously cover the relevant parameter space.

For post-bounce times $t < 1 \text{ s}$, shock effects [1, 8] take place typically at $V > k_H$ and do not significantly affect the H subsystem. The density profile can thus be effectively approximated by its static limit ρ_0 as taken from [1]:

$$t < 1 \text{ s} \quad \rho(x) = \rho_0 \left(\frac{x}{\text{km}} \right)^{2.4} \quad (20)$$

For post-bounce times $t > 1 \text{ s}$, the condition $V = k_H$ can be fulfilled, and the shock profile can thus modulate P_H . We characterize the profile in terms of the shock front position x_s and of its shape variation $f(x)$ (with respect to ρ_0) for both $x < x_s$ and $x > x_s$. Formally, one can write

$$t > 1 \text{ s} \quad \rho(x) = \rho_0(x) \begin{cases} f_<(x) & ; x < x_s \\ 1 & ; x = x_s \\ f_>(x) & ; x > x_s \end{cases} \quad (21)$$

so that $f_>$ can be interpreted as the density enhancement (with respect to ρ_0) at $x = x_s$. Following [1], we take

$$f_>(x) = 10 \quad (22)$$

In Eq. (21), the function $f_<$ parametrizes the rarefaction zone ("hot bubble") above the shock front, characterized by a drop of density over more than one decade in x , and by an asymptotic density increase for $x \gg x_s$. The function $f_>$ characterizes the sudden drop of density below the shock front, down to the static limit. After some trials, we have chosen the following (purely empirical) parametrizations for $f_<$ and $f_>$, which reproduce the main features of the graphical profiles in [1]:

$$\ln f_<(x) = [0.28 - 0.69 \ln(x_s/\text{km})] \left[\arcsin \left(1 - \frac{x - x_s}{x_s} \right)^{1.1} \right] \quad (23)$$

$$f_>(x) = 1 + \frac{1}{1 + \left(\frac{x - x_s}{x_s} \right)^{1.1}} \quad (24)$$

In the above equations, we $x_s \text{ !} = 30$ as default value (unless otherwise stated)⁴ and, following [1], we assume a slightly accelerating shock-front position x_s :

$$x_s(t) = x_s^0 + v_s t + \frac{1}{2} a_s t^2 \quad (25)$$

⁴ Notice that $! = 2 d \ln \rho / d \ln x$ for $x \text{ !} = x_s^+$. Therefore, $!$ basically parametrizes the steepness of the shock front.

with parameters approximately given by

$$x_s^0 \approx 4.6 \cdot 10^3 \text{ km} ; \quad (26)$$

$$v_s \approx 11.3 \cdot 10^3 \text{ km/s} ; \quad (27)$$

$$a_s \approx 0.2 \cdot 10^3 \text{ km/s}^2 ; \quad (28)$$

Notice that the time dependence of $\langle x \rangle$ in Eq. (21) is implicit, through the function $x_s = x_s(t)$. For x far from x_s , it is:

$$\langle x \rangle - x_s \approx \langle x \rangle_0 (x) - 16 (x_s = \text{km})^{1.13} ; \quad (29)$$

$$\langle x \rangle - x_s \approx \langle x \rangle_0 (x) ; \quad (30)$$

Figure 1 shows the neutrino potential $V(x)$ as derived from the above parametrization [Eqs.(20)-(28)] for representative post-bounce times $t = 1$ s, as well as for the static profile ($t = 0$). The solid curves correspond to $\beta = 30$ [default value in Eq. (24)], while the dotted curves correspond to $\beta = 300$ (steeper shock front). These curves reasonably reproduce the main features of the shock profiles from [1]. The horizontal bands represent the ranges where the neutrino potential equals the two wavenumbers ($k_H = V$ and $k_L = V$), for a representative energy interval $E \in [5; 50]$ MeV.

As previously mentioned, a line at constant k_H can intersect the $V(x)$ profile in Fig.1 in at most three points x_i , ordered as $x_1 \leq x_2 \leq x_3$, and corresponding to level crossing probabilities P_1, P_2 , and P_3 . Two of the three intersections merge in the following cases: (1) at the bottom of the rarefaction zone (x_r), where $x_1 = x_2$; (2) at the top of the shock front (x_s), where $x_2 = x_3$. Single transitions can instead occur at early times or high energies ($V(x) = k_H$ at $x = x_3$ only), as well as at late times or low energies ($V(x) = k_H$ only at $x = x_1$). Therefore, the critical cases $V(x_r) = k_H$ ($x_1 = x_2$) and $V(x_s) = k_H$ ($x_2 = x_3$) are expected to mark significant changes in the behavior of P_H .

We conclude this section with several cautionary remarks. At present, there seems to be inconclusive information about the real density gradient just below the shock front. Such gradient (governed, in our simplified parametrization, by the steepness parameter β), is purposely larger in Ref. [1], as compared with Refs. [8]. In fact, the authors of Ref. [1] claim to have steepened the shock front because "... in hydrodynamics calculations [it] may be softened by numerical techniques." No details are given, however, about their corrected steepness (graphically indistinguishable from a vertical density drop in [1]). Since this technical issue is beyond our competence, we have pragmatically adopted a "less-than-vertical" density drop at $x = x_s$ (taking, for definiteness, $\beta = 30$), somehow intermediate between the profiles in [1] and [8]. We will briefly comment on the effect of further increasing the shock front steepness (e.g., by taking $\beta = 300$) and thus the non-adiabatic character of the H⁻ transition. Clearly, the important issue of the density gradient around the shock front should be more properly addressed through dedicated numerical supernova simulations with dense space lattice. A side effect of the shock-front steepening is the appearance of a local "cusp" at $x = x_s$ (as apparent in Ref. [1] and even more in our Fig. 1), which might well be unphysical. However, we do not smooth it out, since it actually provides us with a useful, nontrivial check of numerical versus analytical calculations of P_H in an "extreme" condition (i.e., around a sudden change in the sign and value of the density gradient). Finally, we observe that some "leftover" turbulence might be expected in the rarefaction zone behind the shock front, inducing fuzzy variations of the local density. Such variations might lead to more than three solutions of Eq. (16) in some cases, and thus to a more complicated and

\random " structure for P_H . This possibility (not considered in this work) should be kept in mind when more refined supernova shock simulations will become available.

IV. ANALYSIS OF CROSSING PROBABILITIES IN THE ENERGY DOMAIN

In this Section we study in detail the energy dependence of P_H at fixed time. We pay particular attention to the case of three transitions occurring along the shock density profile.

A. Analytical vs numerical calculations of $P_H(E)$

Figure 2 shows our calculation of $P_H(E)$ at fixed post-bounce time $t = 3.5$ s, for four representative values of $\sin^2 \theta_{13}$ ranging from 10^{-6} (top) to 10^{-3} (bottom). In the left panels, a direct comparison is made between analytical calculations (solid curves) and Runge-Kutta numerical calculations (dots), performed at 4×10^3 equally-spaced points in the interval $E \in [0; 80]$ MeV. As expected from the discussion in the previous section, three different regimes characterize P_H at low, intermediate, and high energy.

For $E < 3.5$ MeV, only one transition occurs ($P_H = P_1$) at relatively high density well behind the shock. Conversely, three transitions occur between $E \approx 3.5$ MeV and $E \approx 42$ MeV, corresponding to the critical points $V(x_s) \approx k_H$ (top of the shock front) and $V(x_r) \approx k_H$ (bottom of the rarefaction zone), respectively.⁵ For $E > 42$ MeV, a single transition occurs ($P_H = P_3$) at low, static density. In the single-transition regimes, the very good agreement between numerical and analytical calculations is evident at a glance in the left panels of Fig. 2. In the intermediate, three-transition regime, the results of the numerical calculations are instead widely scattered around the analytical curve. The reason is that numerical calculations keep track of the phase(s) of the level crossing amplitude(s). For a single amplitude, the associated phase becomes ineffective after taking the squared modulus. For multiple (interfering) amplitudes, instead, the relative phases do provide an oscillating structure in P_H , which is apparent in the numerical results.⁶

In the right panels of Fig. 2, the oscillating structure in the numerical integration is averaged out by a convolution with a Gaussian function (with one-sigma width of 1 MeV), which simulates a generic "smearing" process (e.g., experimental energy resolution). The same convolution is applied to the analytical results. It can be seen that there is very good agreement between the two different (numerical and analytical) approaches after smearing. The small residual wiggles in the numerical results (dotted curves) in the middle panels are actually artifacts, which would disappear by increasing the sampling frequency in the energy domain (not shown). The results of Fig. 2 (and of other checks that we have performed for different post-bounce times) show that analytical calculations of P_H coincide with phase-averaged numerical results with very good accuracy, even close to the "critical" points (top of the shock front and bottom of the rarefaction zone) where two transitions collapse. Moreover, analytical calculations are actually much more convenient than the numerical ones, which require a very high sampling rate in order to perform efficient phase-averaging and to prevent numerical artifacts.

⁵ Notice that these critical points are independent of θ_{13} .

⁶ In the left panels of Fig. 2, for the sake of graphical cleanness, we show the spread of numerical results as scatter plots, rather than through rapidly oscillating curves.

Finally, the energy profiles of P_H in the right panels of Fig. 2 are easily understood for "extreme" values of $\sin^2 \theta_{13}$. For $\sin^2 \theta_{13} = 10^{-6}$, the exponent in Eq. (13) is small enough to make any transition strongly nonadiabatic ($P_i \approx 1 - P_H$). Conversely, all transition probabilities are exponentially suppressed at the "large" value $\sin^2 \theta_{13} = 10^{-3}$ (adiabatic case). For intermediate values of $\sin^2 \theta_{13}$ (10^{-5} and 10^{-4}), the variations of P_H with $\ln E$ are easily understood in the single-transition regimes, where P_H scales as $(\text{const})^{\sin^2 \theta_{13}}$ [see Eq. (13)]. For instance, the high-energy value $P_H \approx 0.88$ at $\sin^2 \theta_{13} = 10^{-5}$ drops to $P_H \approx (0.88)^{10} = 0.28$ for a tenfold increase in $\sin^2 \theta_{13}$. In the multiple-transition regime, instead, each probability P_i scales as $(\text{const})^{\sin^2 \theta_{13}}$, while the overall probability P_H from Eq. (19) does not. In this case, P_H is better understood by separating its components P_i , as we do in the next subsection.

B. $P_H(E)$ decomposition

Figure 3 shows the decomposition of $P_H(E)$ (analytical, unsmoothed) into the three crossing probabilities $P_{1,2,3}$ at $t = 3.5$ s, for $\sin^2 \theta_{13} = 10^{-5}$ (top panel) and $\sin^2 \theta_{13} = 10^{-4}$ (bottom panel). The various transition probabilities are switched on and off at the two critical energies $E \approx 3.5$ MeV and $E \approx 42$ MeV, as previously discussed.

In the top panel of Fig. 3, both P_1 and P_3 are strongly nonadiabatic (≈ 1), and thus $P_H \approx P_1 \approx 1$ and $P_H \approx P_3 \approx 1$ in the single-transition regimes at low and high energy, respectively. At intermediate energies P_2 is nonzero, but its nonadiabatic character is less pronounced, since at x_2 (outer part of the rarefaction zone), the density gradient is smaller [and the scale factor in Eq. (12) is larger] than at x_1 or x_3 | at least in our simplified description of the density profile. Therefore, in this intermediate energy regime, the strong nonadiabaticity of both P_1 and P_3 implies $P_H \approx P_2$ through Eq. (19). In summary, in the top panel of Fig. 3, the overall crossing probability P_H basically takes the values P_1 , P_2 , and P_3 as the energy increases and passes through its two critical values. All relevant parts of the density profile (shock front and both sides of the rarefaction zone) can thus contribute to the P_H energy profile.

In the bottom panel of Fig. 3, the higher value of $\sin^2 \theta_{13}$ leads to an overall decrease of the nonadiabaticity, particularly for the second transition ($P_2 \approx 0$). Therefore, P_H basically takes the values P_1 , $(P_1 + P_3 - 2P_1P_3)$, and P_3 , as the energy increases. The details of the outer part of the rarefaction zone (just behind the shock front) are not relevant in this case.

Summarizing, variations of $\sin^2 \theta_{13}$ for fixed density profile can modulate significantly the relative contributions to the crossing probability P_H , which are governed by the shape of the shock front and of the rarefaction zone. When θ_{13} will be known, one shall be able to gauge the relative importance of such contributions, and to determine which parts of the shock profile should be most intensively studied. In the meantime, all parts of the shock profile should be considered as potentially important and worth further study.

C. $P_H(E)$ variations for different steepness and times

We conclude the analysis in the energy domain by briefly discussing the variations of $P_H(E)$ (analytical, unsmoothed) originated by: (1) Variations of the shock steepness β , and (2) variations of the post-bounce time t .

Figure 4 shows the function $P_H(E)$ at $t = 3.5$ s and $\sin^2 \theta_{13} = 10^{-4}$ (top panel) and 10^{-3} (bottom panel), for three different values of the steepness parameter $!$ [Eq. 24)]. For increasing values of $!$, the crossing probabilities P_1 and P_2 are unaffected, while P_3 becomes increasingly nonadiabatic in the energy range where k_H probes the shock front from top to bottom (notice that this range decreases for increasing $!$, see Fig. 1). This feature can lead to a "bump" in P_H (bottom panel) or to a faster variation of P_H in the energy domain (top panel), according to the value of $\sin^2 \theta_{13}$. We have verified that, by taking even larger (and possibly unphysical) steepness values ($! = 10^3$, i.e., almost "vertical" shock front), also the "low" crossing probability P_L could become nonzero (at later times). Determining a physically acceptable range for the front steepness is thus an important issue, which should be addressed by future supernova simulations.

Finally, Fig. 5 shows the function $P_H(E)$ at three different times for $\sin^2 \theta_{13} = 10^{-5}$ (top panel) and 10^{-4} (bottom panel). The curves at $t = 4$ s are not much different from the cases previously discussed in this section ($t = 3.5$ s). At earlier times $t < 1$ s ($t = 0$ s in Fig. 5) the behavior of P_H is simpler, being basically dictated by the static profile. At later times ($t = 8$ s), the critical energies at which $k_H = V(x_s)$ and $k_H = V(x_r)$ move forward, the latter falling outside the shown energy range. As a consequence, the nonadiabatic character of the innermost transition at x_1 makes $P_H \approx 1$ in about the first half of the energy range of Fig. 5, with a rapid drop to smaller values as the more adiabatic transition P_2 becomes relevant. The drift of the zones where P_H is high or low has thus an interesting time structure, which is analyzed in more detail in the next section.

V. ANALYSIS OF CROSSING PROBABILITIES IN THE TIME DOMAIN

In this Section we study in detail the time dependence of P_H at fixed energy. As in Sec. IV, we start with a comparison between numerical and analytical calculations of P_H , and then study the decomposition of P_H in terms of $P_{1,2,3}$.

A. Analytical vs numerical calculations of $P_H(t)$

Figure 6 shows our calculation of $P_H(t)$ at fixed neutrino energy $E = 30$ MeV, for four representative values of $\sin^2 \theta_{13}$ ranging from 10^{-6} (top) to 10^{-3} (bottom). In the left panels, a direct comparison is made between analytical calculations (solid curves) and Runge-Kutta numerical calculations (dots), performed at 5×10^3 equally-spaced points in the interval $t \in [0; 12]$ s. In analogy to the previous discussion in the energy domain, also the time structure of P_H is characterized by three different regimes. These regimes are separated by two "critical times," namely, $t' = 3$ s (when k_H equals V at the bottom of the rarefaction zone x_r) and $t' = 8$ s (when k_H equals V at the top of the shock front x_s).⁷ For increasing t , P_H is thus governed by P_3 only, then by $P_{1,2,3}$, and finally by P_1 only.

At intermediate times, when all P_i 's are effective, phase effects show up in the numerical calculations, leading to a significant scatter of the results around the average (left panels in Fig. 6). Phase averaging (smearing) is enforced in the right panels, through a convolution

⁷ Notice that, for about one second before the first of these two critical times, k_H probes also V at the bottom of the shock front.

with a "top-hat" resolution function with 0.25 s width. It can be seen that numerical and analytical calculation are in very good agreement at all times, up to small residual artifacts in the smoothed numerical results, which would disappear by sampling the abscissa more densely (not shown). In conclusion, Figs. 2 and 6 demonstrate that simple, analytical calculations provide the correct phase-averaged value of P_H as a function of both E and t . These reassuring results show that time-consuming numerical estimates of neutrino transitions along the shock profile [1, 8] can be accurately replaced by much faster and elementary calculations.

The functions $P_H(t)$ in Fig. 6 show significant variations with $\sin^2 \theta_{13}$. In the top panel, $\sin^2 \theta_{13}$ is sufficiently small to make all transitions strongly nonadiabatic and $P_H \approx 1$. The single-transition values of P_H at early and late times are reduced by successive powers of ten as $\sin^2 \theta_{13}$ is increased by factors of ten from top to bottom, in analogy with the discussion of Fig. 2. At intermediate times, when three transitions take place, a decomposition of P_H into $P_{1,2,3}$ is instead necessary to grasp its main features.

B. $P_H(t)$ decomposition

Figure 7 shows the decomposition of $P_H(t)$ (analytical, unsmoothed) into the three crossing probabilities $P_{1,2,3}$ at $E = 30$ MeV, for $\sin^2 \theta_{13} = 10^{-5}$ (top panel) and $\sin^2 \theta_{13} = 10^{-4}$ (bottom panel). The various transition probabilities are switched on and off at the two critical times $t' = 3$ s and $t' = 8$ s. In the top panel, P_3 and P_1 dominate at early and late times, while the drop of P_H at intermediate times is dominated by the probability P_2 . In the bottom panel, each of the three probabilities is suppressed by a power of ten, leading to strong suppression of P_2 , and to a leading dependence of P_H on P_1 and P_3 only. The results in this figure confirm that variations of θ_{13} can lead to dramatic variations in the role of each P_i (and thus of different parts of the shock profile) in building the final crossing probability P_H as a function of both energy and time.

VI. IMPACT ON OBSERVABLE POSITRON SPECTRA

As an application of the analytical calculation of P_H described in the previous section, we study the effect of the shock propagation on the energy (and time) spectra of positrons detectable at the Earth through the inverse beta-decay reaction



We assume a "standard" supernova explosion at $D = 10$ kpc, releasing a total energy $E_B = 3 \times 10^{53}$ erg, equally shared among the (anti)neutrino flavors, and distributed in time as

$$L(t) = \frac{E_B}{6} e^{-t/\tau} \quad ; \quad (32)$$

where L is the luminosity for each flux, and the decay time is taken as $\tau = 3$ s [1]. For the sake of simplicity, we assume unpinched (normalized) Fermi-Dirac spectra with time-independent temperatures T ,

$$f(E) = \frac{0.176}{T^4} \frac{L(t)}{4 D^2} \frac{E^2}{e^{E/T} + 1} \quad ; \quad (33)$$

where we take $T_{\bar{\nu}_e} = 4.5 \text{ M eV}$ and $T_{\bar{\nu}_\mu} = 6.5 \text{ M eV}$ ($x = \bar{\nu}_\mu; \bar{\nu}_e$).⁸

In the presence of oscillations, the supernova $\bar{\nu}_e$ spectrum is given by

$$f(E) = f_{\bar{\nu}_e}(E)P_{ee} + f_{\bar{\nu}_\mu}(E)(1 - P_{ee}); \quad (34)$$

where P_{ee} is taken from Eq. 15 (antineutrino case). The convolution of $f(E)$ with the differential cross section $d\sigma(E; E_{\text{pos}}) = dE_{\text{E_pos}}$ [22] provides the event spectrum $dN = dE_{\text{E_pos}}$ in terms of the positron energy E_{pos} . We assume perfect energy resolution and zero threshold, in order to show the shock effects in the most favorable conditions. It is understood that such effects will be somewhat degraded in realistic cases, depending on detector details. Finally, just to fix the overall scale, we assume a detector volume corresponding to 32 kton of water (as in the Super-Kamiokande experiment). However, for the main purposes of our discussion, the event rate units could be taken as arbitrary in the following figures.

Figure 8 shows our calculated positron spectra for no oscillations ($P_{ee} = 1$, dashed curve) and hypothetical full conversion ($P_{ee} = 0$, dot-dashed curve). For partial conversion, Eq. (33) implies that the final positron spectrum is basically a linear combination of the previous two spectra. Examples are given in Fig. 8 for $\sin^2 \theta_{13} = 10^{-5}$, for both normal hierarchy (dotted curve) and inverted hierarchy (solid curve). For normal hierarchy, the coefficients of the combination are energy-independent, namely, $P_{ee} = \cos^2 \theta_{12}$ and $1 - P_{ee} = \sin^2 \theta_{12}$ [see Eq. (15)]. Conversely, for inverse hierarchy, such coefficients become energy- and time-dependent through P_H [$P_{ee} = \cos^2 \theta_{12} P_H(E)$]. In the specific example of Fig. 8, the time is fixed through integration over a representative bin $t = 6 - 0.25 \text{ s}$. The energy profile of $P_H(E)$ then governs the relative weight of the spectra $f_{\bar{\nu}_e}$ and $f_{\bar{\nu}_\mu}$ in the combination. As the energy increases and P_H drops (see Fig. 5 and related comments), the weight of $f_{\bar{\nu}_\mu}$ suddenly increases and the positron spectrum is shifted to higher energies. The "shoulder" around peak of the solid curve is thus an imprint of the shock passage. This shoulder is expected to drift as we choose time bins different from $t = 6 - 0.25 \text{ s}$.

Figure 9 shows a set of successive positron energy spectra, binned in time intervals of 0.5 s, from about 6 to 9 seconds after bounce. The overall decrease of the spectra for increasing t is due to the decrease in luminosity. The top panel does not include Earth effects, while the bottom panels includes representative Earth mantle crossing effects, calculated in the same conditions as in [19]. As in Fig. 8, the cases of normal and inverted hierarchy are distinguished through dotted and solid curves, respectively, and $\sin^2 \theta_{13}$ is fixed at 10^{-5} . The top panel shows how the shock passage can leave an observable, time-dependent spectral deformation, in the case of inverse hierarchy. This possibility is very exciting, although one might realistically hope to see no more than variations in the first (or maybe second) spectral moment [8, 10].

From the comparison of the top and bottom panel in Fig. 9, it turns out that the spectral modulation due to the shock might be partly hindered, at late times, by the additional modulation generated by Earth effects. In other words, the "wiggles" produced by oscillations in the Earth might make it difficult to identify the position of the genuine, shock-dependent spectral deformations at different times. Therefore, in some cases Earth effects may not necessarily represent an additional handle [10] to study the shock dynamics via neutrinos.

Finally, Fig. 10 shows the drop in the positron event rate (arbitrary units) as a function of time, for $\sin^2 \theta_{13} = 10^{-5}$. Four rates are displayed, integrated over consecutive 10 MeV

⁸ For recent discussions of supernova neutrino energy spectra, see [13, 14].

energy bins. For normal hierarchy, the rates decrease according to the (assumed) exponential law in Eq. (32). For inverted hierarchy, the characteristic time structure of $P_H(t)$ (see the top panel in Fig. 7) is reflected in a characteristic deviation of the rate decrease with respect to a pure exponential drop. Signatures of this kind have been emphasized in [1]. It goes without saying that very high statistics would be needed to discriminate such time structure in real experiments.⁹

VII. SUMMARY AND PROSPECTS

Supernova shock propagation can produce interesting effects in the energy and time structure of the neutrino signal, as suggested in [1] and also investigated in [8, 10]. In the calculation of such effects for 3 oscillations, the neutrino crossing probability P_H in the 1-3 neutrino subsystem plays an important role. The evaluation of P_H can be done either numerically or analytically, for given shock profiles in space and time. By assuming a simplified description of the time-dependent density profile, we have explicitly shown that simple analytical calculations accurately reproduce the phase-averaged numerical results, also in the nonobvious case of multiple transitions along the shock profile. The analytical approach has then been used to study some relevant characteristics of the structure of P_H in energy and time. This structure can in part be reflected in observable event spectra, as we have shown through some simple and selected examples.

The simplifications used in this work, and especially the empirical parametrization of the density profile, do not alter our main conclusions about the validity and usefulness of a simple analytical approach to P_H , as compared with brute-force numerical calculations. However, such simplifications may affect the specific values of P_H that we have estimated at given energy and time. These values (and the corresponding observable effects) should not be taken too literally, since they depend on features of the shock profile which are beyond our control. In particular, the physical range for the shock front steepness (and, to some extent, for the shape of the rarefaction zone) should be restricted, if possible, by dedicated supernova simulations with higher resolution in space and time. When such issues will be clarified, more realistic calculations of P_H , and of its imprint on observable neutrino signals at the Earth, will become possible.

⁹ A more complete and quantitative study of the observability of shock-induced structures in neutrino signals will be performed elsewhere, in the context of future large-volume, high-statistics detectors.

Acknowledgments

This work was in part supported by the Italian Ministero dell'Istruzione, Università e Ricerca (MIUR) and Istituto Nazionale di Fisica Nucleare (INFN) within the "Astroparticle Physics" research project. We thank Cecilia Lunardini for useful comments on the manuscript. One of us (E.L.) acknowledges kind hospitality at the Institute for Advanced Study (Princeton, NJ) where this work was completed.

-
- [1] R.C. Schirato and G.M. Fuller, "Connection between supernova shocks, flavor transformation, and the neutrino signal," astro-ph/0205390.
 - [2] Simulations of supernova shock propagation over 20 s have been performed by J.R. Wilson and H.E. Dalhed, as quoted in [1].
 - [3] G.G. Raelt, in the Proceedings of the International School of Physics "Enrico Fermi," Course 152 (Varenna, Lake Como, Italy, 2002), to appear [hep-ph/0208024].
 - [4] J.F. Beacom, in the Proceedings of "Neutrino 2002," 20th International Conference on Neutrino Physics and Astrophysics (Munich, Germany, 2002), to appear [astro-ph/0209136].
 - [5] J. Engel, G.C.M. Laughlin, and C. Volpe, Phys. Rev. D 67, 013005 (2003) [hep-ph/0209267].
 - [6] S. Ando and K. Sato, astro-ph/0210502.
 - [7] S. Ando and K. Sato, Phys. Rev. D 67, 023004 (2003) [hep-ph/0211053].
 - [8] K. Takahashi, K. Sato, H.E. Dalhed, and J.R. Wilson, astro-ph/0212195.
 - [9] S. Choubey and K. Kar, hep-ph/0212326.
 - [10] C. Lunardini and A. Yu. Smimov, hep-ph/0302033.
 - [11] L. Wolfenstein, Phys. Rev. D 17, 2369 (1978); S.P. Mikheev and A. Yu. Smimov, Yad. Fiz. 42, 1441 (1985) [Sov. J. Nucl. Phys. 42, 913 (1985)].
 - [12] R. Buras, M. Rampp, H.T. Janka, and K. Kifonidis, astro-ph/0303171.
 - [13] M.T. Keil, G.G. Raelt and H.T. Janka, astro-ph/0208035.
 - [14] G.G. Raelt, M.T. Keil, R. Buras, H.T. Janka, and M. Rampp, astro-ph/0303226.
 - [15] Particle Data Group Collaboration, K. Hagiwara et al., Phys. Rev. D 66, 010001 (2002).
 - [16] G.L. Fogli, E. Lisi, A. Marrone, D. Montanino, A. Palazzo, and A.M. Rotunno, hep-ph/0212127.
 - [17] G.L. Fogli, E. Lisi, A. Marrone, and D. Montanino, hep-ph/0303064.
 - [18] T.K. Kuo and J. Pantaleone, Rev. Mod. Phys. 61, 937 (1989).
 - [19] G.L. Fogli, E. Lisi, D. Montanino, and A. Palazzo, Phys. Rev. D 65, 073008 (2002); (E) 66, 039901 (2002).
 - [20] A.S. Dighe and A. Yu. Smimov, Phys. Rev. D 62, 033007 (2000).
 - [21] C.S. Lim, K. Ogure, and H. Tsujimoto, Phys. Rev. D 67, 033007 (2003).
 - [22] A. Strumia and F. Vissani, astro-ph/0302055.

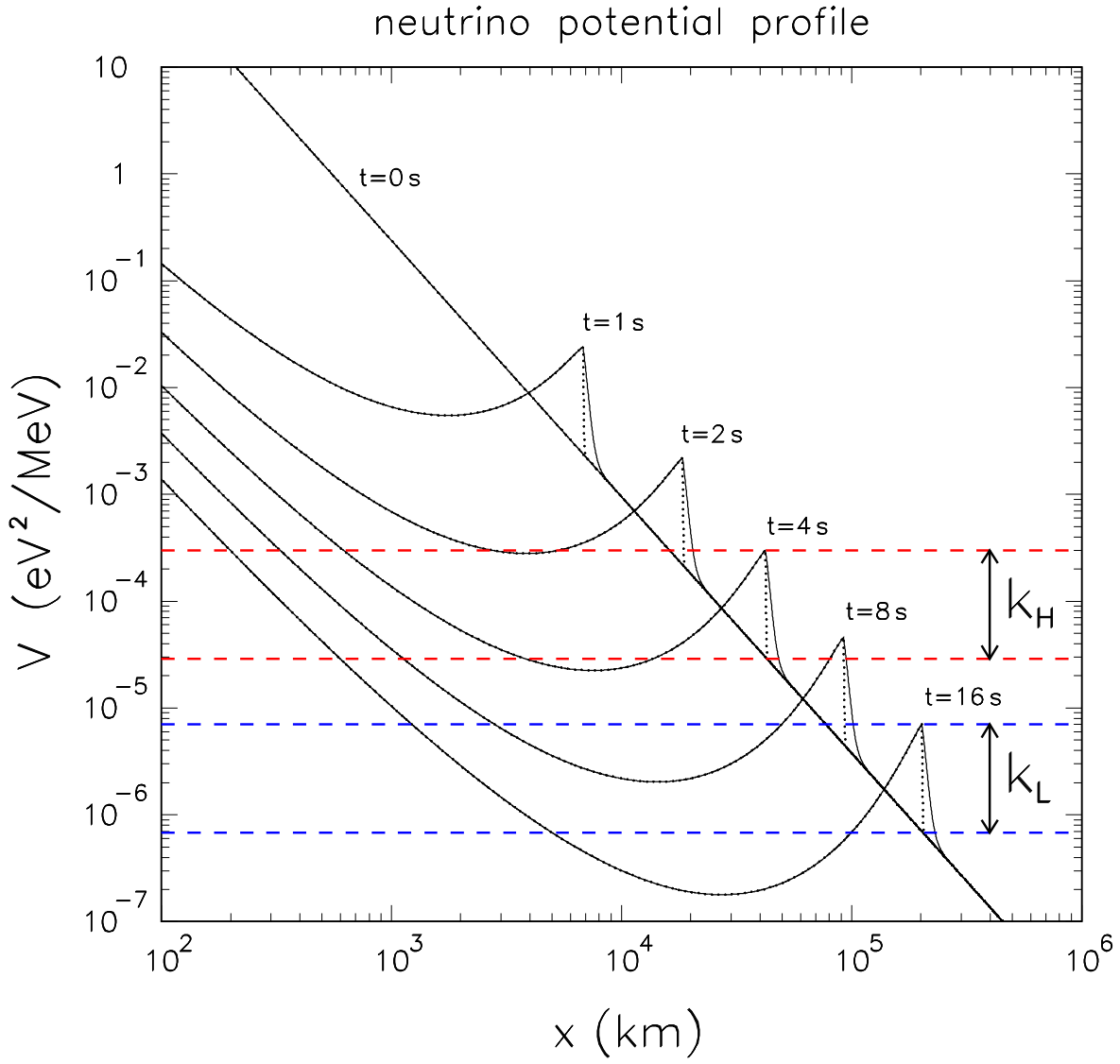


FIG . 1: Neutrino potential V in terms of the supernova radius x , for different values of the post-bounce time t , as derived from our simplified parametrization of the profiles in [1]. The solid and dotted lines correspond to steepness parameter $\beta = 30$ (default) and $\beta = 300$, respectively. The horizontal bands represent typical ranges of the neutrino wavenumbers k_H and k_L . See the text for details.

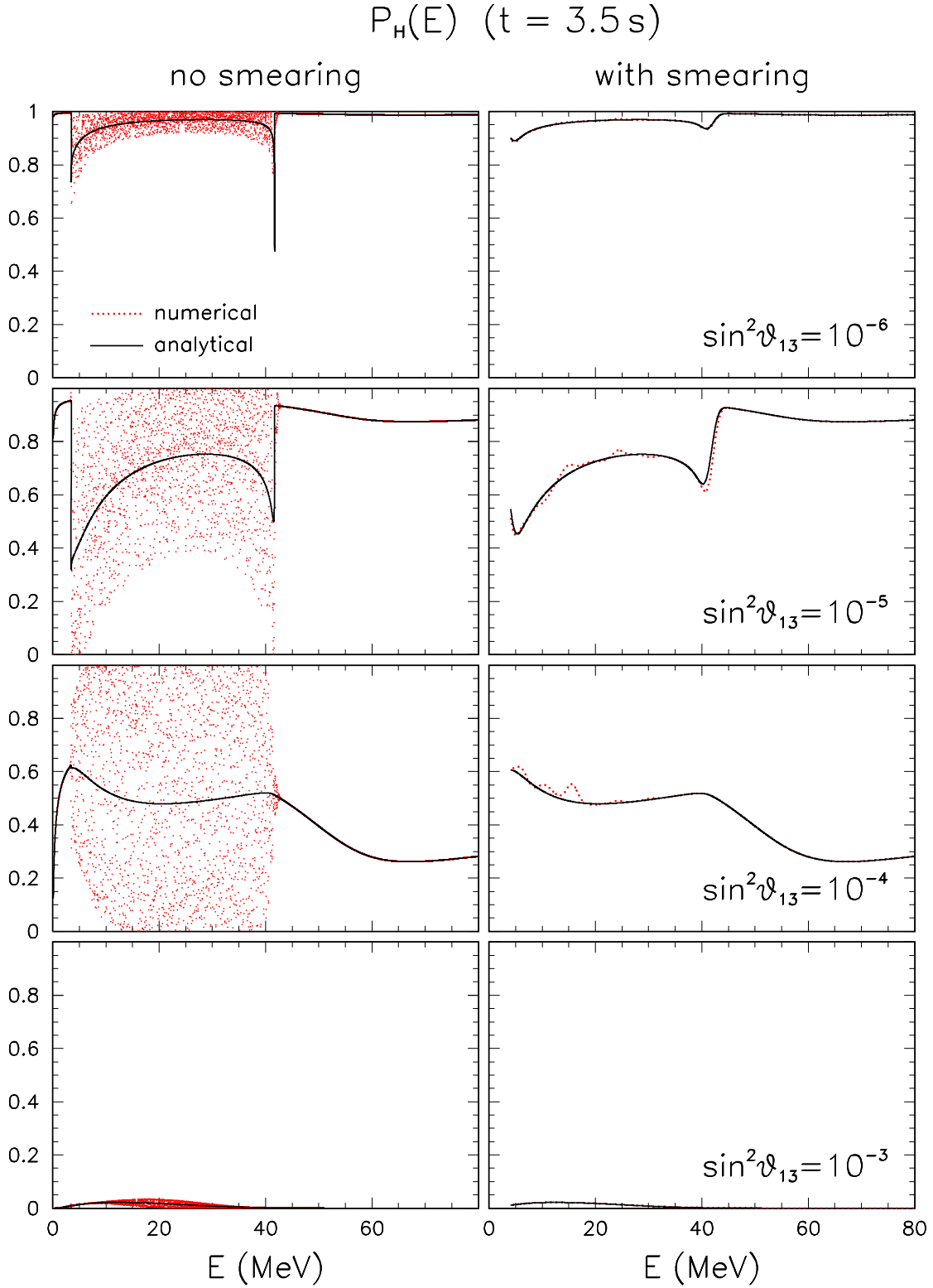


FIG . 2: Comparison of numerical and analytical calculations of the crossing probability $P_H(E)$ (dots and solid curves, respectively) at $t = 3.5$ s, for representative values of $\sin^2 \vartheta_{13}$. In the right panels, phase effects are energy-averaged.

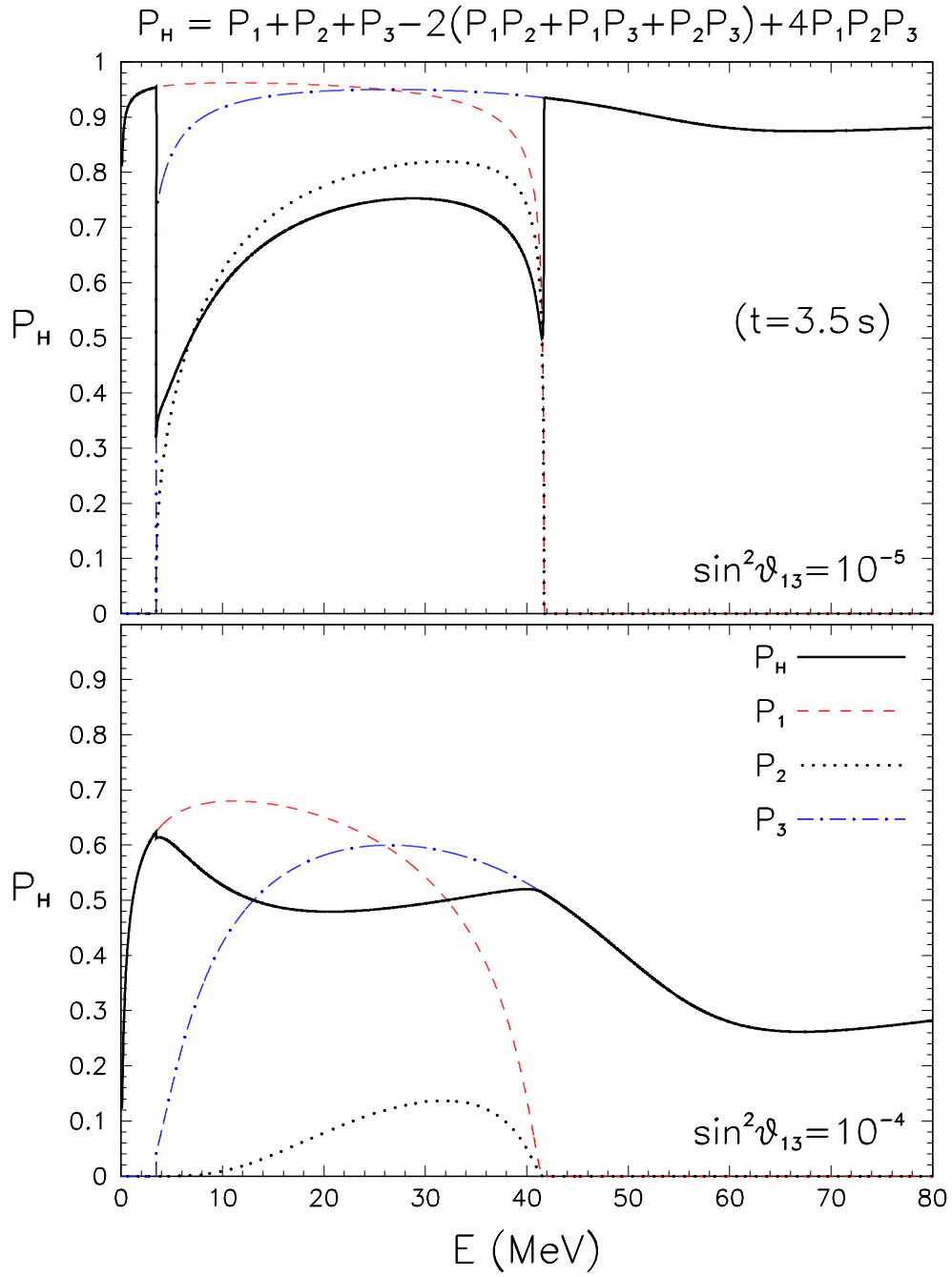


FIG. 3: $P_H(E)$ in terms of its components $P_{1,2,3}$ at $t = 3.5$ s, for two representative values of $\sin^2 \theta_{13}$.

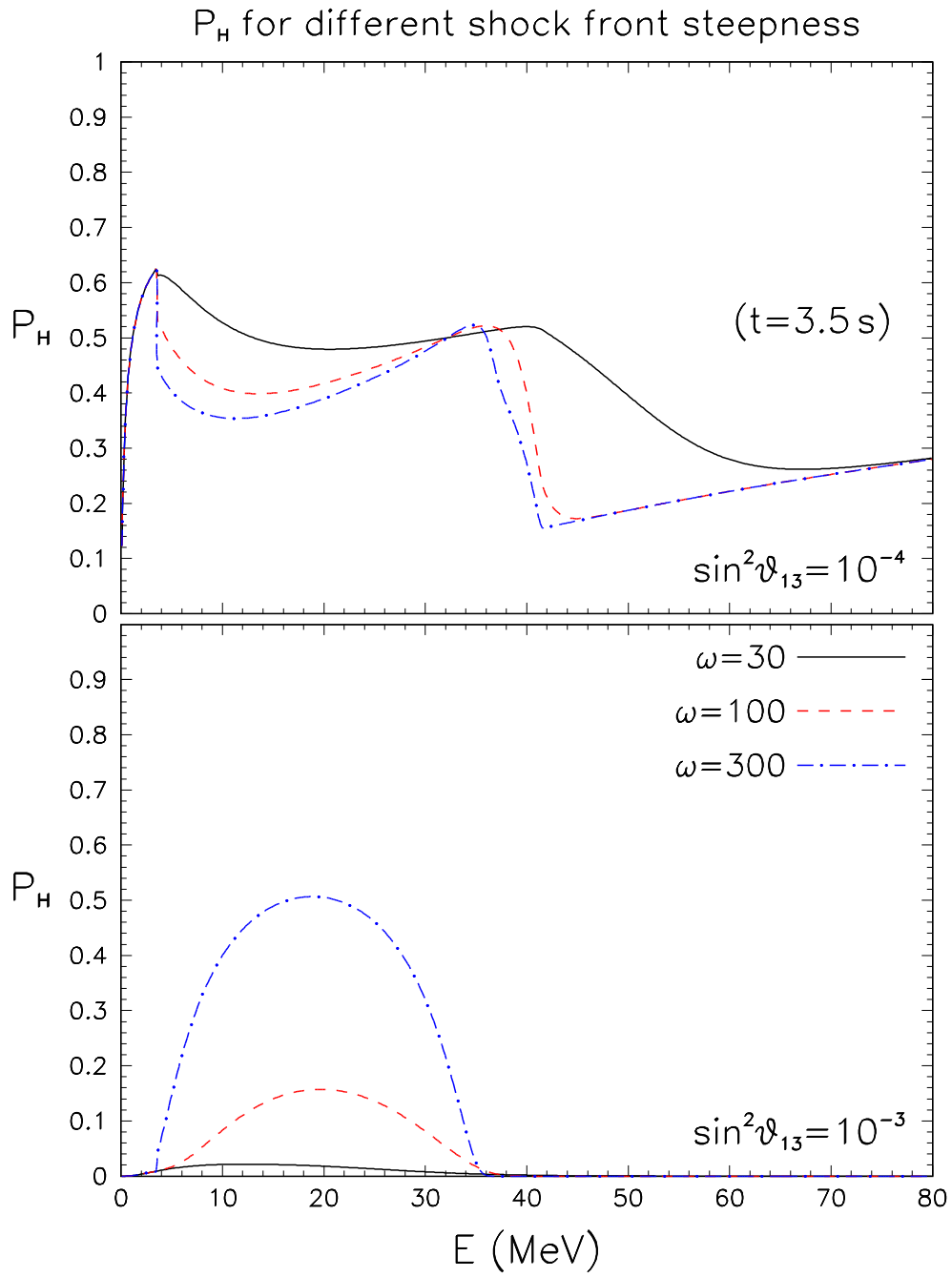


FIG .4: $P_H(E)$ at $t = 3.5$ s, for two representative values of $\sin^2 \theta_{13}$ and for different shock-front steepness values.

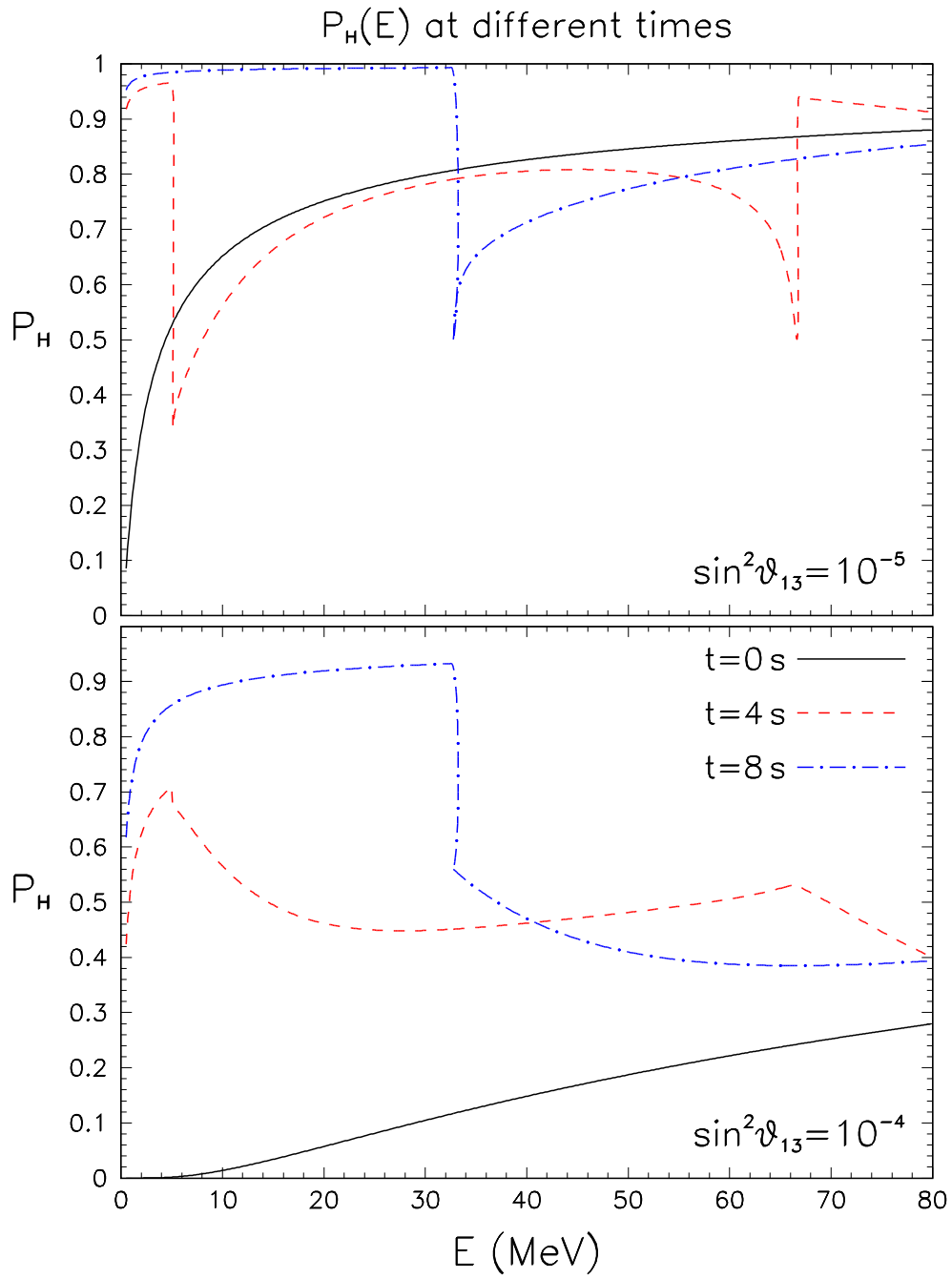


FIG. 5: $P_H(E)$ at $t = 0, 4,$ and 8 s, for two representative values of $\sin^2 \theta_{13}$.

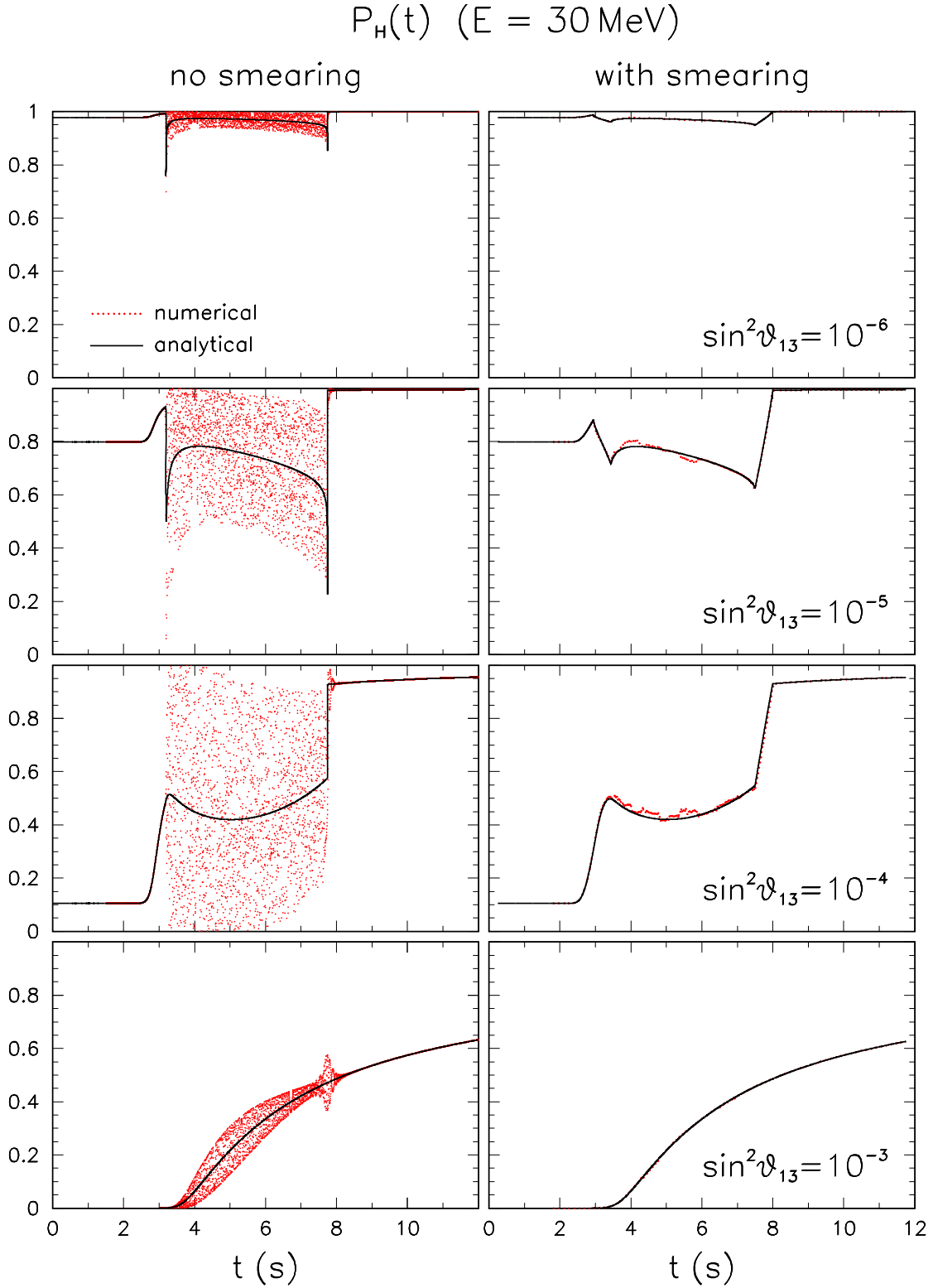


FIG . 6: Comparison of numerical and analytical calculations of the crossing probability $P_H(t)$ (dots and solid curves, respectively) at $E = 30 \text{ MeV}$, for representative values of $\sin^2 \vartheta_{13}$. In the right panels, phase effects are time-averaged.

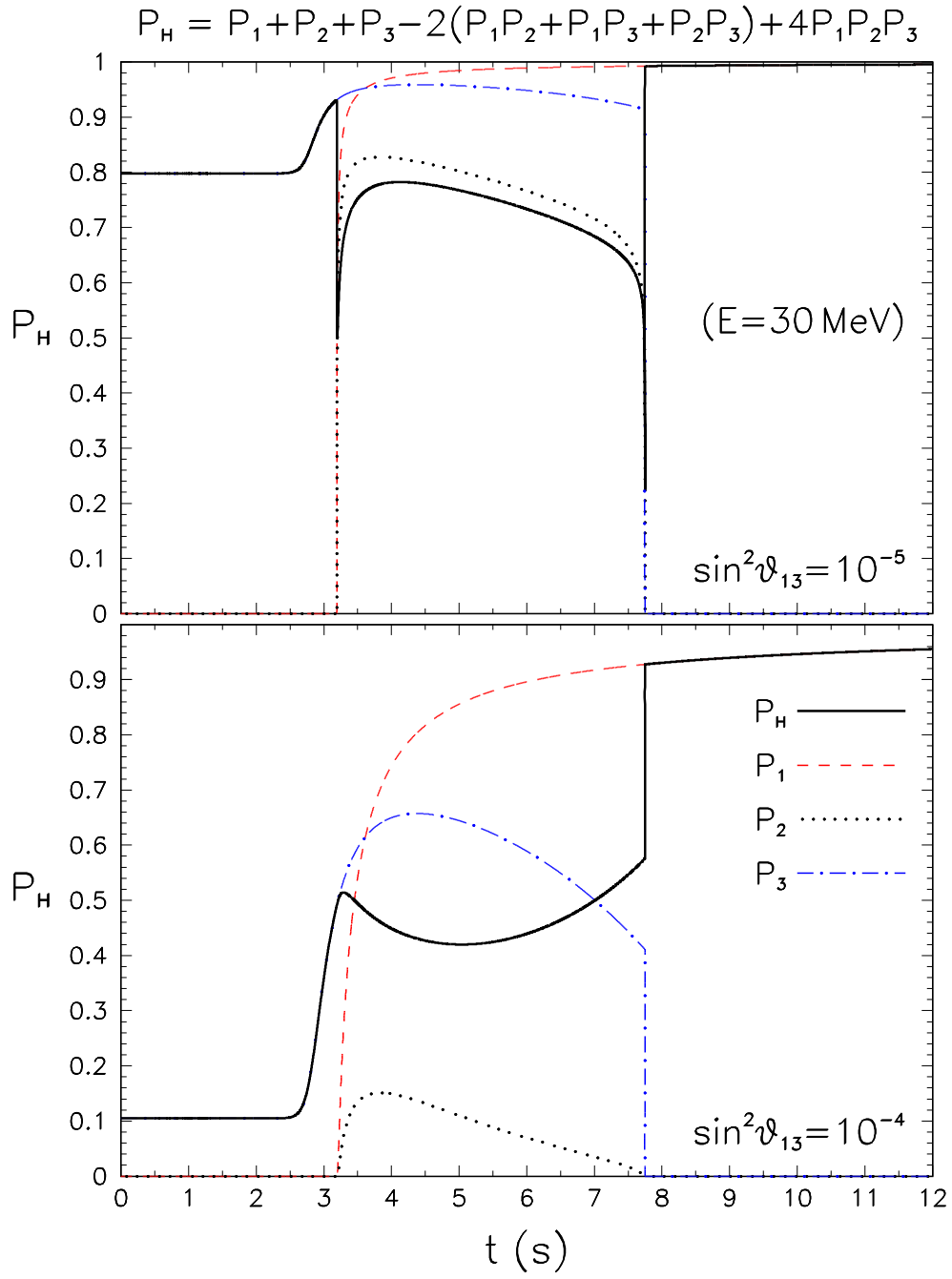


FIG. 7: $P_H(t)$ in terms of its components $P_{1;2;3}$ at $t = 3.5$ s, for two representative values of $\sin^2 \theta_{13}$.

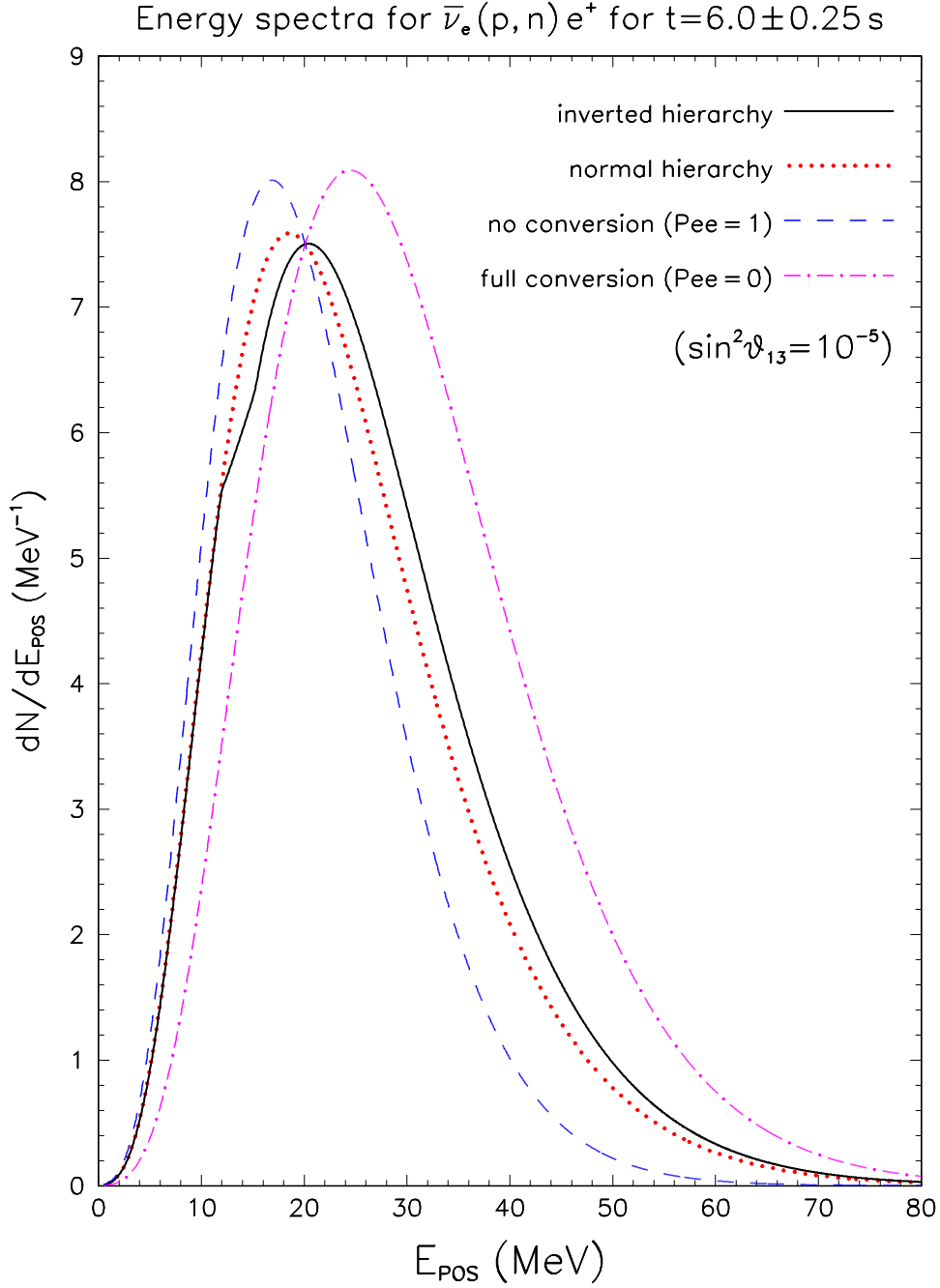


FIG .8: Representative positron energy spectra of supernova antineutrino events from inverse beta decay, for different degrees of $\bar{\nu}_e$ conversion into $\bar{\nu}_x$. Dashed curve: No conversion. Dot-dashed curve: Full conversion. Dotted line: Partial conversion for normal hierarchy. Solid line: Partial conversion for inverse hierarchy. The latter case shows the shock imprint in the range $E \sim 10\{20$ MeV, calculated for $\sin^2 \theta_{13} = 10^{-5}$, and integrated over time interval $t = 6 \pm 0.25$ s.

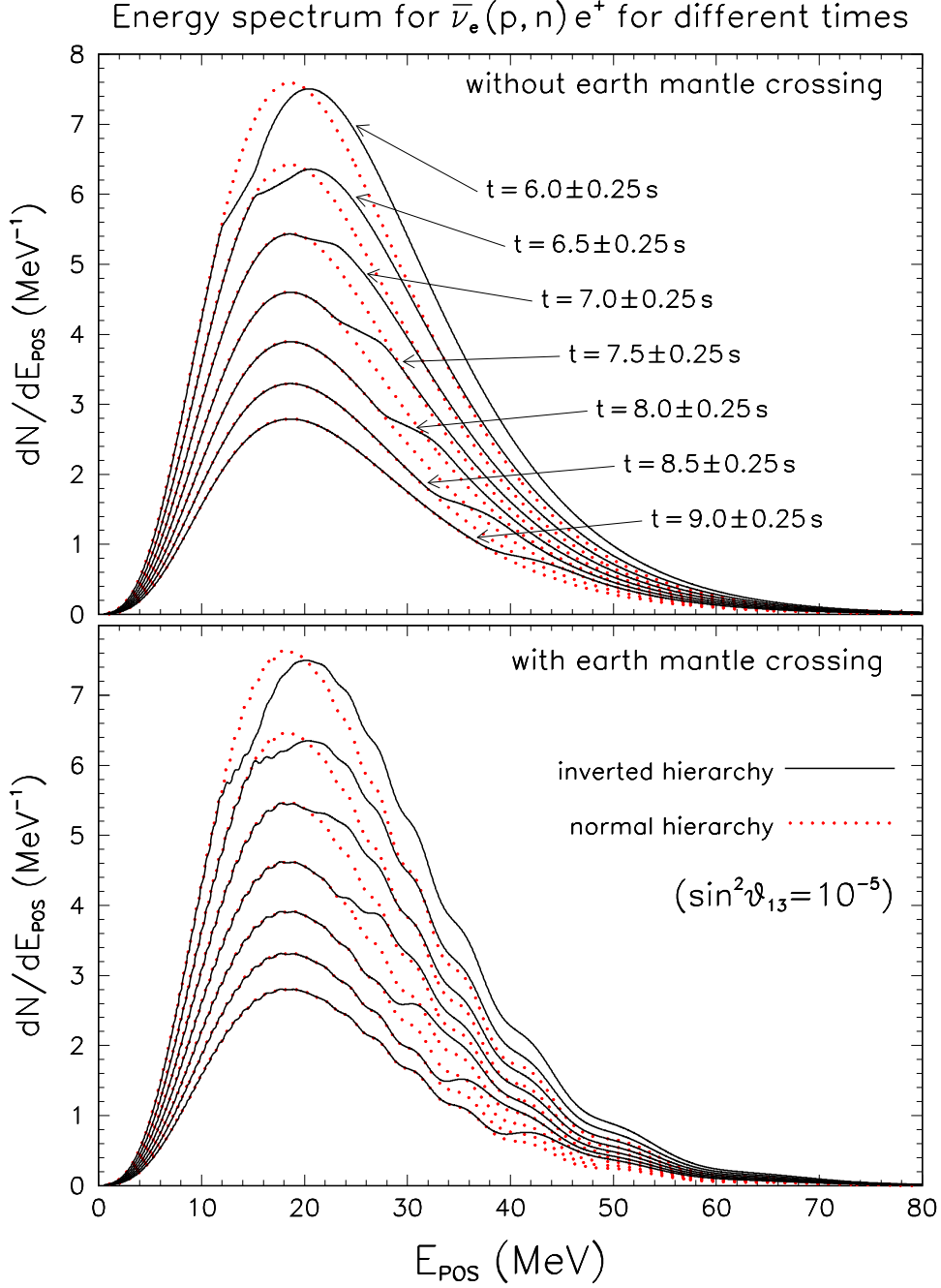


FIG. 9: Positron energy spectra for successive time bins, calculated for $\sin^2 \theta_{13} = 10^{-5}$ and for normal and inverted hierarchy (dotted and solid curves, respectively). In the case of inverted hierarchy, shock-induced spectral deformation move forward in energy for increasing post-bounce time. The bottom panel includes representative effects of Earth mantle crossing, which induce additional spectral deformations.

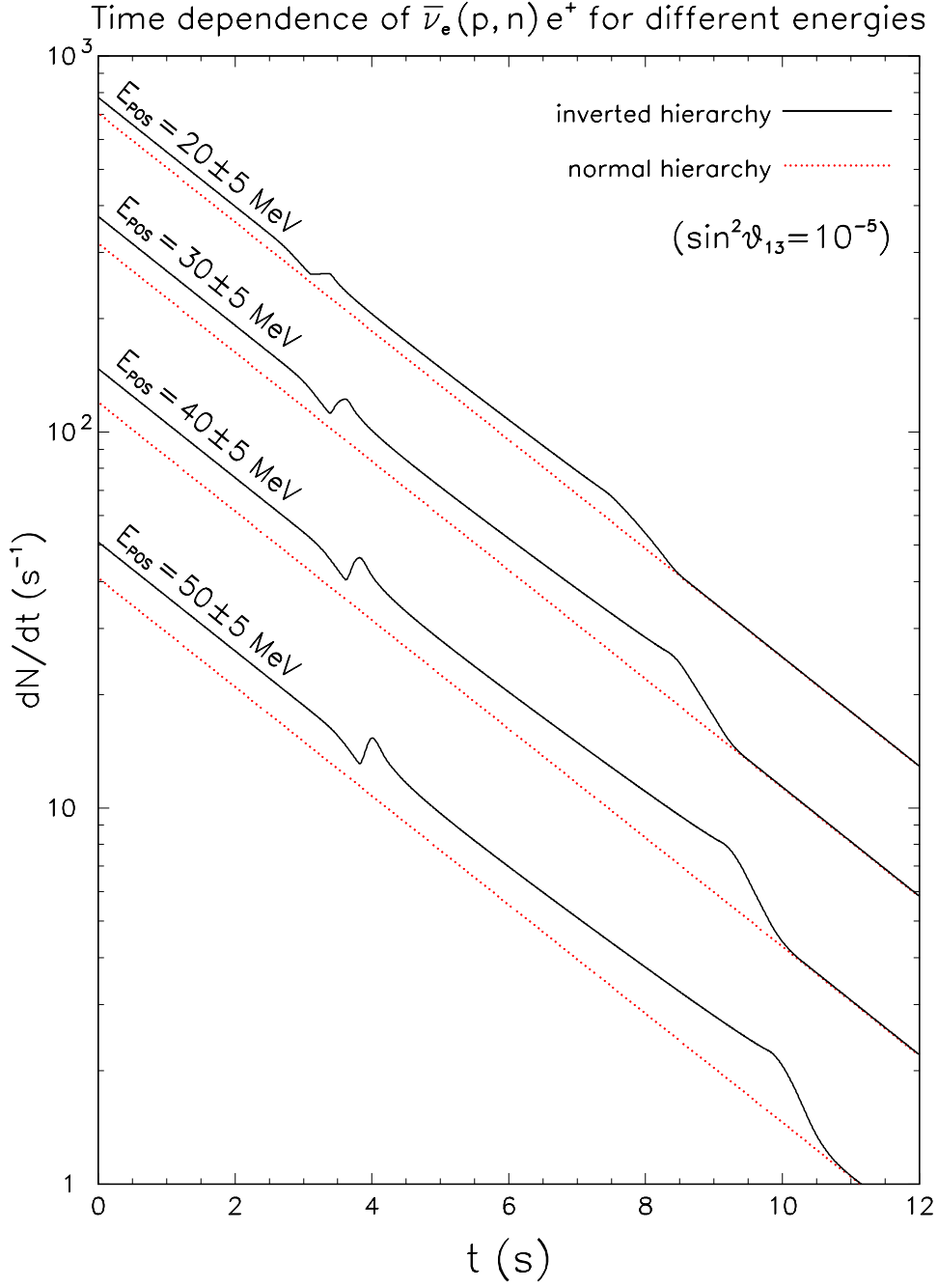


FIG .10: Time dependence of the positron event rate for $\sin^2 \theta_{13} = 10^{-5}$ and four different energy intervals. For normal hierarchy (dotted lines), the rate is just proportional to the neutrino luminosity (assumed to decay exponentially in time). For inverted hierarchy (solid lines) an additional time structure is induced by the shock propagation.